Supplementary Information

Enhanced generation of internal tides under global warming

Authors: Zhibin Yang[1], Zhao Jing[1, 2], Xiaoming Zhai[3], Clément Vic[4], Hui Sun[2], Casimir de Lavergne[5], Man Yuan[2]

Affiliations:

[1]Laoshan Laboratory, Qingdao, China.

[2]Frontier Science Center for Deep Ocean Multispheres and Earth System (FDOMES) and Physical Oceanography Laboratory, Ocean University of China, Qingdao, China.

[3]Centre for Ocean and Atmospheric Sciences, School of Environmental Sciences, University of East Anglia, Norwich, United Kingdom.

[4]University of Brest, CNRS, Ifremer, IRD, Laboratoire d'Océanographie Physique et Spatiale (LOPS), IUEM, Plouzané, France.

[5]LOCEAN Laboratory, Sorbonne Université/IRD/CNRS/MNHN, Paris, France

Corresponding author: Zhao Jing (jingzhao@ouc.edu.cn)

Supplementary Note 1

Response of Atlantic meridional overturning circulation to the increased energy conversion into high-mode internal tides

We analyze the change of the Atlantic meridional overturning circulation (AMOC) in response to the 8% increase of $E^{4\text{-}50}$. This is done by running a pair of numerical simulations based on a global OGCM (Parallel Ocean Program version 2; POP2) with a tidal mixing parameterization for high-mode internal tides[1]. The OGCM has a nominal horizontal resolution of 1° and 60 layers vertically and is driven by the climatological atmospheric forcing constructed from the NCEP–NCAR reanalysis[2], GXGXS precipitation data set[3] and GISS radiation model[4]. The OGCM is initialized from rest and spun up for 600 years to reach a quasi-equilibrium state. The $E^{4\text{-}50}$ in the tidal mixing parameterization is obtained from the empirical formula proposed by St Laurent et al.[1]. Then two experiments (Exp-Historical and Exp-Future) are branched off and run for another 1000 years. They share the same setting except that $E^{4\text{-}50}$ in Exp-Historical and Exp-Future are replaced by the historical (1995-2014) and future (2091-2100) mean values estimated in this study (Fig. 2c and f). In other words, the globally integrated $E^{4\text{-}50}$ in the Exp-Future is 8% higher than that in the Exp-Historical.

Supplementary Note 2

Response of dianeutral upwelling to the increased energy conversion into high-mode internal tides

We analyze the effects of 8% increase of $E^{4\text{-}50}$ on the dianeutral upwelling that is important for the formation of deep water[5]. The dianeutral upwelling transport is calculated following the method of de Lavergne et al.[6]:

$$T\left(\gamma^{n}\right)=\iint_{A\left(\gamma^{n}\right)}\frac{\partial F}{\partial\gamma^{n}}dA \quad (1)$$

where γ^{n} is the neutral density, F is the neutral density flux, and the integral is computed over the isosurface of γ^{n} (denoted as $A(\gamma^{n})$). The F is defined as:

$$F=-\int_{-H}^{z_{A\left(\gamma^{n}\right)}}\left[b\frac{\partial\rho}{\partial\Theta}\frac{\partial}{\partial z}\left(\kappa_{\rho}\frac{\partial\Theta}{\partial z}\right)+b\frac{\partial\rho}{\partial S_{\mathrm{A}}}\frac{\partial}{\partial z}\left(\kappa_{\rho}\frac{\partial S_{\mathrm{A}}}{\partial z}\right)\right]dz \quad (2)$$

where H is the sea water depth, $z_{A\left(\gamma^{n}\right)}$ is the vertical coordinate of $A(\gamma^{n})$, the factor $b=\partial_{\perp}\gamma^{n}/\partial_{\perp}\rho$ with $\partial_{\perp}$ is the gradient along the diapycnal direction, ρ is the potential density, Θ is the conservative temperature, S_{A} is the absolute salinity, and κ_{ρ} is the parameterized turbulent diffusivity induced by breaking of high-mode internal tides[1].

To analyze the effects of 8% increase of high-mode tidal energy conversion on $T\left(\gamma^{n}\right)$, we fix the γ^{n}, Θ and S_{A} as their climatological mean values derived from the WOCE hydrographic atlas[7] and vary the high-mode tidal energy conversions in the tidal mixing parameterization.

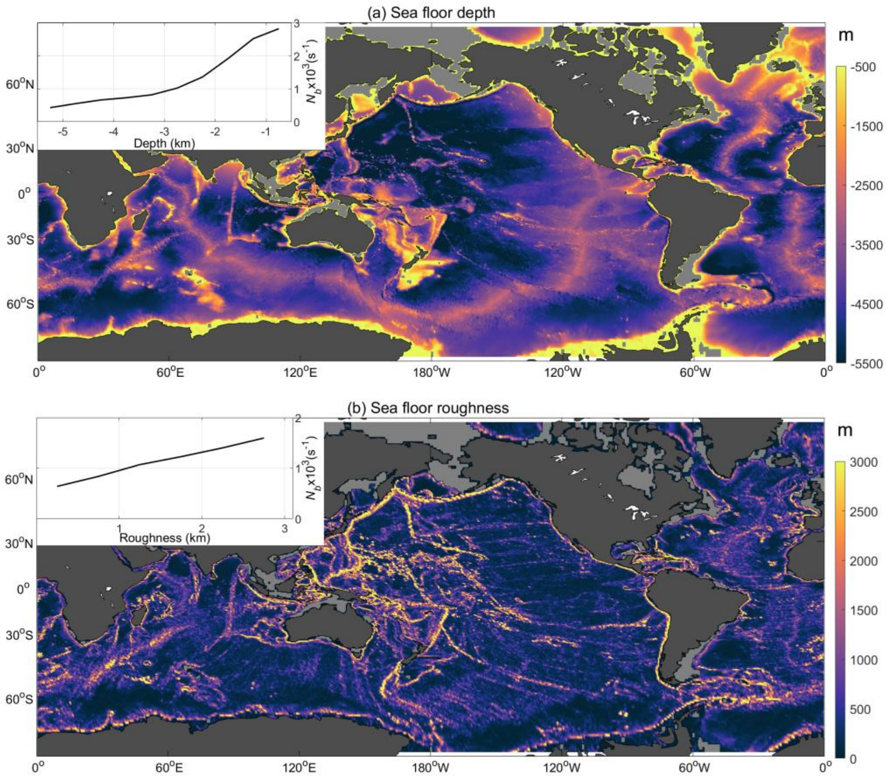

Supplementary Fig. 1. Dependence of near-bottom buoyancy frequency on sea floor depth and roughness. Global distribution of sea floor depth **(a)** and roughness **(b)**. Inserted panels show the bin-averaged near-bottom buoyancy frequency N_b as a function of sea floor depth **(a)** and sea floor roughness **(b)**.

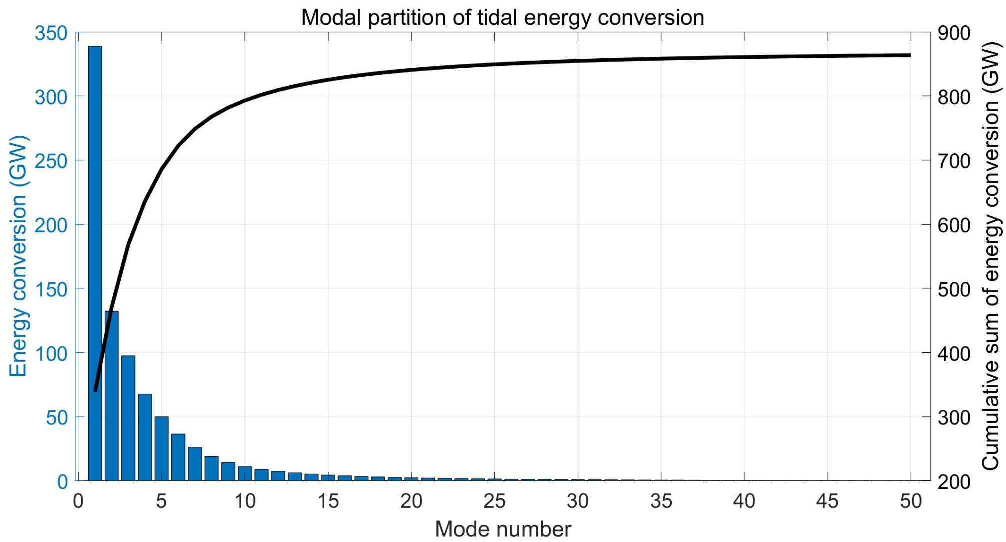

Supplementary Fig. 2. Energy conversion into internal tides of different modes. Globally integrated tidal energy conversion into different modes during 1995-2004.

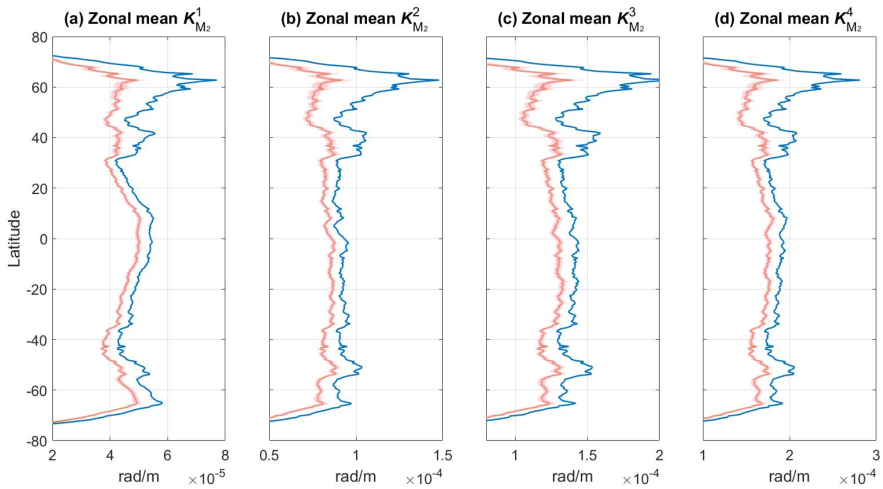

Supplementary Fig. 3. Response of modal horizontal wavenumber of M_2 internal tides to global warming. a, Zonal mean mode-1 horizontal wavenumber of M_2 internal tides during 1995-2004 (blue) and 2091-2100 (red). Color shading represents the 95% confidence interval. **b-d,** Same as **a,** but for the mode 2, mode 3 and mode 4, respectively.

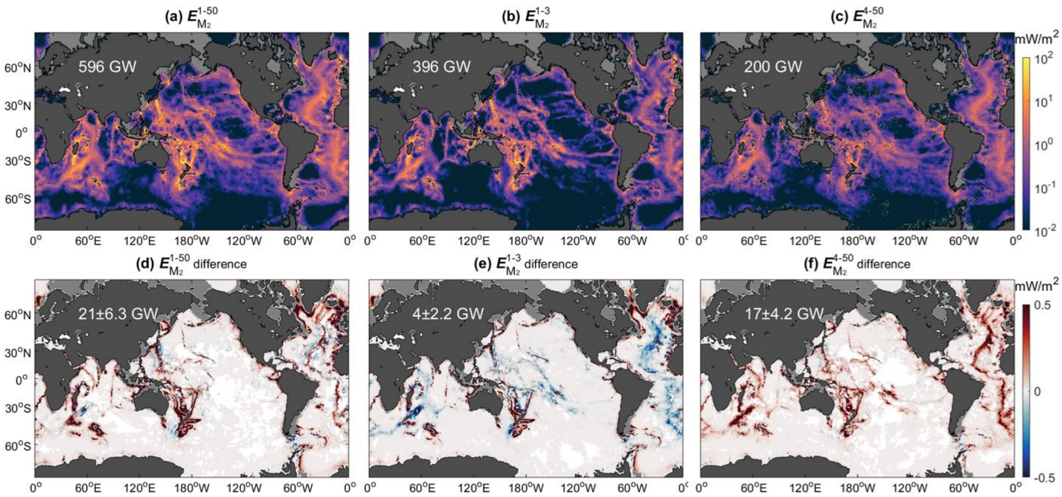

Supplementary Fig. 4. Response of M_2 tidal energy conversion and its modal partition to global warming. Same as Fig. 2 but for the M_2 internal tides alone.

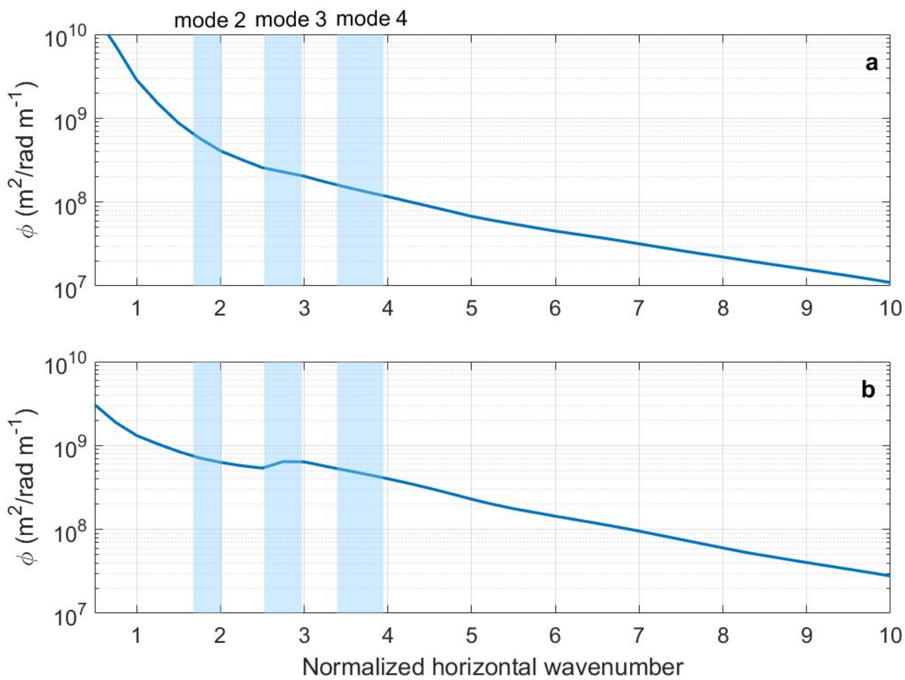

Supplementary Fig. 5. Effects of topographic spectrum on the response of tidal energy conversion to global warming. Topographic spectrum (ϕ) as a function of horizontal wavenumber normalized by the mode-1 horizontal wavenumber of M_2 internal tides $K^1_{M_2}$ during 1995-2004, averaged over the regions with the increased **(a)** and decreased **(b)** $E^{1\text{-}3}$ under global warming. The colored shadings denote the interquartile ranges of $K^2_{M_2}/K^1_{M_2}$, $K^3_{M_2}/K^1_{M_2}$ and $K^4_{M_2}/K^1_{M_2}$.

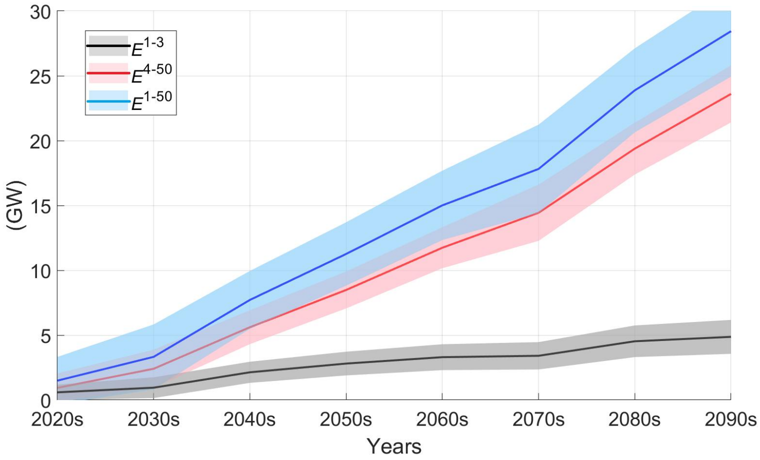

Supplementary Fig. 6. Projected changes of globally integrated tidal energy conversion under different time periods. Changes of the total tidal energy conversion E^{1-50} (blue) and its partition into low modes E^{1-3} (black) and high modes E^{4-50} (red), relative to the time-mean values during 1995-2004. The color shadings represent their 95% confidence intervals.

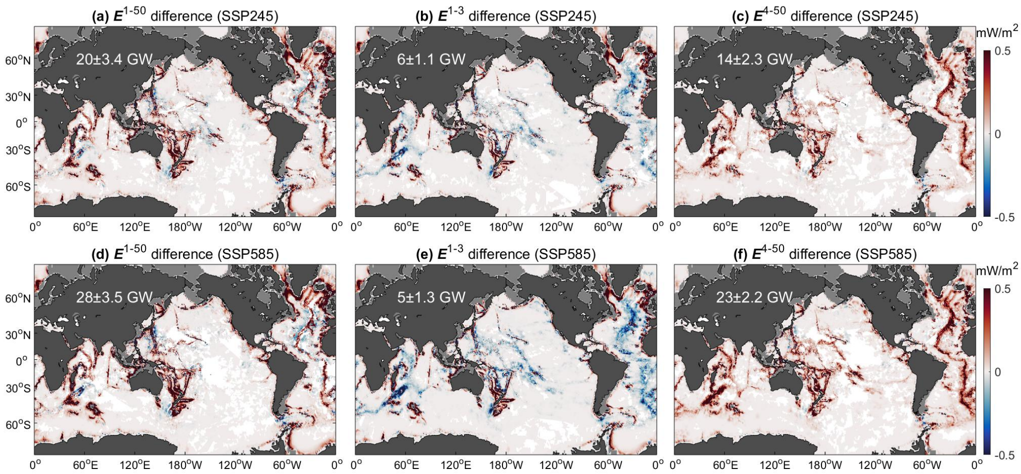

Supplementary Fig. 7. Response of tidal energy conversion and its modal partition to global warming under the SSP245 and SSP585. a-c, Geographical distribution of projected changes (2091-2100 minus 1995-2004) of total tidal energy conversion E^{1-50} (a), and its partition into low modes $E^{1\text{-}3}$ (b) and high modes $E^{4\text{-}50}$ under the SSP245 scenario (c). **d-f,** Same as **a-c,** but under the SSP585 scenario. Changes insignificant at a 95% confidence level are filled in white. Numbers in white represent the globally integrated values as well as their 95% confidence interval.

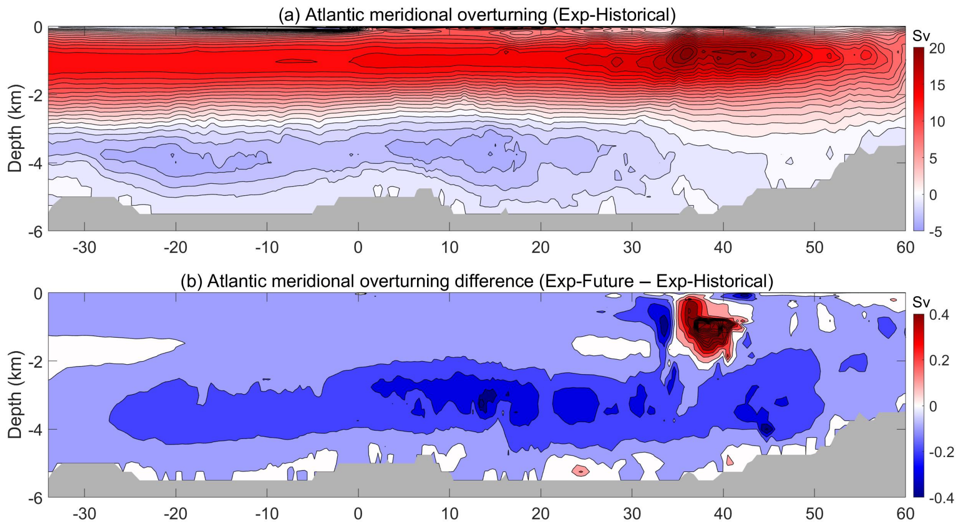

Supplementary Fig. 8. Response of the Atlantic meridional overturning circulation (AMOC) to the increase of energy conversion into high-mode internal tides. a, Time-mean AMOC in the Exp-Historical. **b,** Difference of AMOC between Exp-Historical and Exp-Future (the latter minus the former). Please see Supplementary Note 1 for more details.

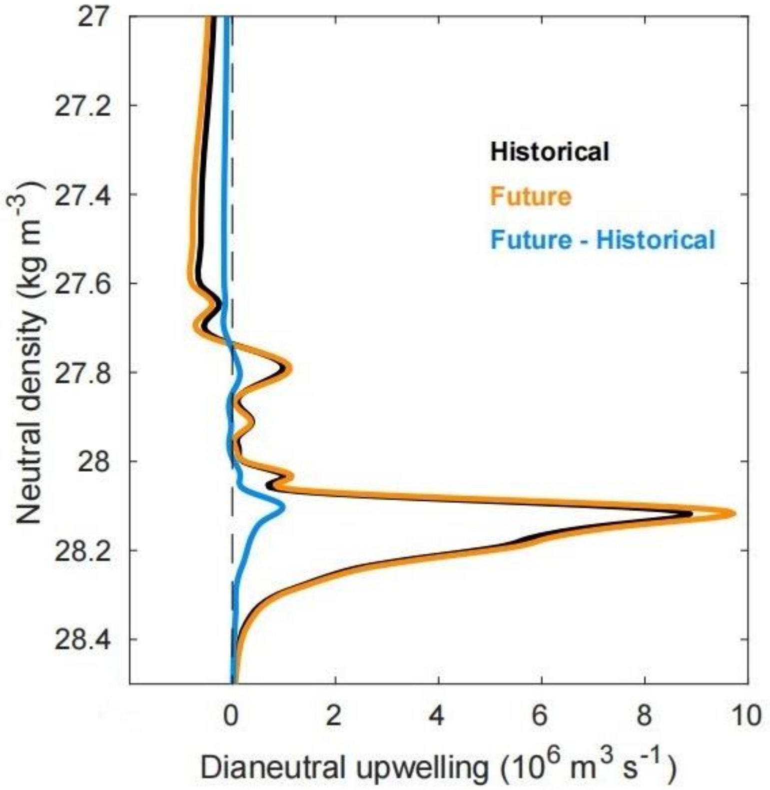

Supplementary Fig. 9. Response of dianeutral upwelling to the increase of energy conversion into high-mode internal tides. Black and yellow lines represent the globally integrated $T\left(\gamma^n\right)$ calculated using the historical (1995-2014) and future (2091-2100) high-mode tidal energy conversions in the tidal mixing parameterization, with the blue line representing their difference (future minus historical). Please see Supplementary Note 2 for more details.

Supplementary Table 1. A list of CMIP6 CGCMs used in this study.

CMIP6	Oceanic Resolution	Scenario
1. ACCESS-CM2	100 km	PI-CTRL, SSP5-8.5, SSP2-4.5
2. CAMS-CSM1-0	100 km	PI-CTRL, SSP5-8.5, SSP2-4.5
3. CanESM5	100 km	PI-CTRL, SSP5-8.5, SSP2-4.5
4. CanESM5-1	100 km	PI-CTRL, SSP5-8.5, SSP2-4.5
5. CESM2	100 km	PI-CTRL, SSP5-8.5, SSP2-4.5
6. CESM2-WACCM	100 km	PI-CTRL, SSP5-8.5, SSP2-4.5
7. CIESM	50 km	PI-CTRL, SSP5-8.5, SSP2-4.5
8. CMCC-ESM2	100 km	PI-CTRL, SSP5-8.5, SSP2-4.5
9. CNRM-CM6-1	100 km	PI-CTRL, SSP5-8.5, SSP2-4.5
10. CNRM-CM6-1-HR	25 km	PI-CTRL, SSP5-8.5, SSP2-4.5
11. E3SM-1-0	50 km	PI-CTRL, SSP5-8.5
12. EC-Earth3-Veg-LR	100 km	PI-CTRL, SSP5-8.5, SSP2-4.5
13. GFDL-ESM4	50 km	PI-CTRL, SSP5-8.5, SSP2-4.5
14. GISS-E2-1-G	100 km	PI-CTRL, SSP5-8.5, SSP2-4.5
15. HadGEM3-GC31-LL	100 km	PI-CTRL, SSP5-8.5, SSP2-4.5
16. HadGEM3-GC31-MM	25 km	PI-CTRL, SSP5-8.5
17. IPSL-CM6A-LR	100 km	PI-CTRL, SSP5-8.5, SSP2-4.5
18. MIROC-ES2L	100 km	PI-CTRL, SSP5-8.5, SSP2-4.5
19. MIROC6	100 km	PI-CTRL, SSP5-8.5, SSP2-4.5
20. MPI-ESM1-2-HR	50 km	PI-CTRL, SSP5-8.5, SSP2-4.5
21. MPI-ESM1-2-LR	250 km	PI-CTRL, SSP5-8.5, SSP2-4.5
22. MRI-ESM2-0	100 km	PI-CTRL, SSP5-8.5, SSP2-4.5
23. NESM3	100 km	PI-CTRL, SSP5-8.5, SSP2-4.5
24. NorESM2-LM	100 km	PI-CTRL, SSP5-8.5, SSP2-4.5
25. UKESM1-0-LL	100 km	PI-CTRL, SSP5-8.5, SSP2-4.5

Supplementary References:

1. St Laurent, L., Simmons, H. & Jayne, S. Estimating tidally driven mixing in the deep ocean. Geophys. Res. Lett. 29, 21-1–21-4 (2002).

2. Kalnay, E. et al. The NCEP/NCAR 40-year reanalysis project. Bull. Am. Meteorol. Soc. 77, 437－471 (1996).

3. Large, W. G. & Yeager, S. G. Diurnal to Decadal Global Forcing For Ocean And Sea-ice Models: The Data Sets And Flux Climatologies (National Center for Atmospheric Research, Boulder, 2004).

4. Zhang, Y-C., Rossow, W. B., Lacis, A. A., Oinas, V. & Mishchenko, M. I. Calculation of radiative fluxes from the surface to top of atmosphere based on ISCCP and other global data sets: Refinements of the radiative transfer model and the input data. J. Geophys. Res. 109, D19105 (2004).

5. Munk, W. & Wunsch, C. Abyssal recipes II: energetics of tidal and wind mixing. Deep-Sea Res. I 45, 1977–2010 (1998).

6. de Lavergne, C., Madec, G., Le Sommer, J., Nurser, A. J. G. & Naveira Garabato, A. C. On the consumption of Antarctic Bottom Water in the abyssal ocean. J. Phys. Oceanogr. 46, 635–661 (2016).

7. Gouretski, V. & Koltermann, K. P. WOCE global hydrographic climatology. Berichte des BSH 35, 1–52 (2004).